

Dimensionality Modulates Electrical Conductivity in Compositionally Constant One-, Two-, and Three-Dimensional Frameworks

Tianyang Chen, Jin-Hu Dou, Luming Yang, Chenyue Sun, Julius J. Oppenheim, Jian Li,* and Mircea Dinca*



Cite This: <https://doi.org/10.1021/jacs.2c00614>



Read Online

ACCESS |



Metrics & More

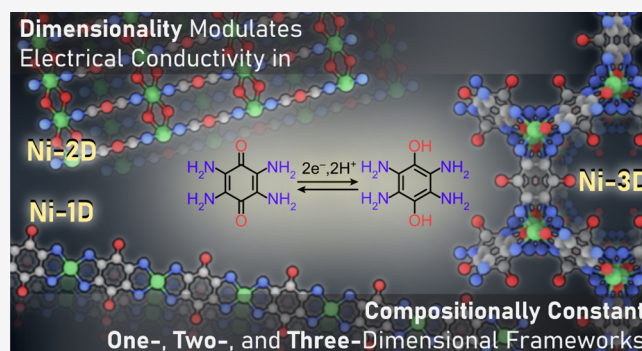


Article Recommendations



Supporting Information

ABSTRACT: We reveal here the construction of Ni-based metal–organic frameworks (MOFs) and conjugated coordination polymers (CCPs) with different structural dimensionalities, including closely π -stacked 1D chains (Ni-1D), aggregated 2D layers (Ni-2D), and a 3D framework (Ni-3D), based on 2,3,5,6-tetraamino-1,4-hydroquinone (TAHQ) and its various oxidized forms. These materials have the same metal–ligand composition but exhibit distinct electronic properties caused by different dimensionalities and supramolecular interactions between SBUs, ligands, and structural motifs. The electrical conductivity of these materials spans nearly 8 orders of magnitude, approaching 0.3 S/cm.



INTRODUCTION

Interest in electrically conducting metal–organic frameworks (MOFs)^{1,2} and nonporous conjugated coordination polymers (CCPs)^{3,4} is growing, not least because they have shown potential applications as active materials for supercapacitors,^{5–8} batteries,^{9–12} electrocatalysis,^{13–15} chemiresistive sensors,^{16–18} thermoelectrics,^{19,20} and superconductors,^{21,22} among others. Electrical conductivities that span more than 10 orders of magnitude have been reported for these materials, but systematic advances in understanding structure–function relationships in this class are rare, even when similar building blocks are employed. For instance, use of the common hexahydroxytriphenylene (HHTP) or hexaiminotriphenylene (HITP) ligands leads to some of the highest electrical conductivities (>100 S/cm),^{23,24} but also very low conductivities (<10^{−7} S/cm).²⁵ Evidently, these vast differences are related to both structure and composition. Whereas identical structures with different compositions naturally give rise to different electrical properties,^{15,26–28} probing the opposite, that is, how electrical properties change when the composition is constant but the structure changes, has not been possible thus far.

Here, we employ 2,3,5,6-tetraamino-1,4-hydroquinone (TAHQ) and its various oxidized forms to isolate three distinct porous and nonporous Ni-based frameworks that share the same 1:1 metal/ligand ratio, but exhibit structures with one-, two-, and three-dimensional connectivities (Figure 1c). Their electrical conductivities span nearly 8 orders of magnitude, reaching 0.3 S/cm.

RESULTS AND DISCUSSION

Ligand Choice. Several features of TAHQ are attractive from a coordination standpoint. In its most reduced form, TAHQ is essentially a hydroquinone with two 1,2-phenylenediamine moieties on either side of the phenol groups. Electron-rich TAHQ readily oxidizes to produce the quinone form tetraaminobenzoquinone (TABQ, Figures 1a and S1; see Supporting Information for synthetic details). Whereas both phenol and amino groups can engage in metal coordination in TAHQ, the significantly reduced electron density of the quinone groups makes them poor ligands, and TABQ typically coordinates metals only through its amino groups (Figure 1b). Electrostatic potential (ESP) surfaces of the two redox partners (Figure 1a) highlight additional distinguishing features that arise in TABQ upon oxidation: a significantly reduced HOMO–LUMO gap relative to TAHQ (Figure S2) and a reduced electron density on the quinone carbons.²⁹ These establish donor–acceptor (D–A) interactions that could further influence the framework structure, as is the case in molecular TABQ crystals (Figure S1, Table S1).³⁰ Indeed, D–A alignment is often used to tailor the solid-state packing of conducting

Received: January 17, 2022

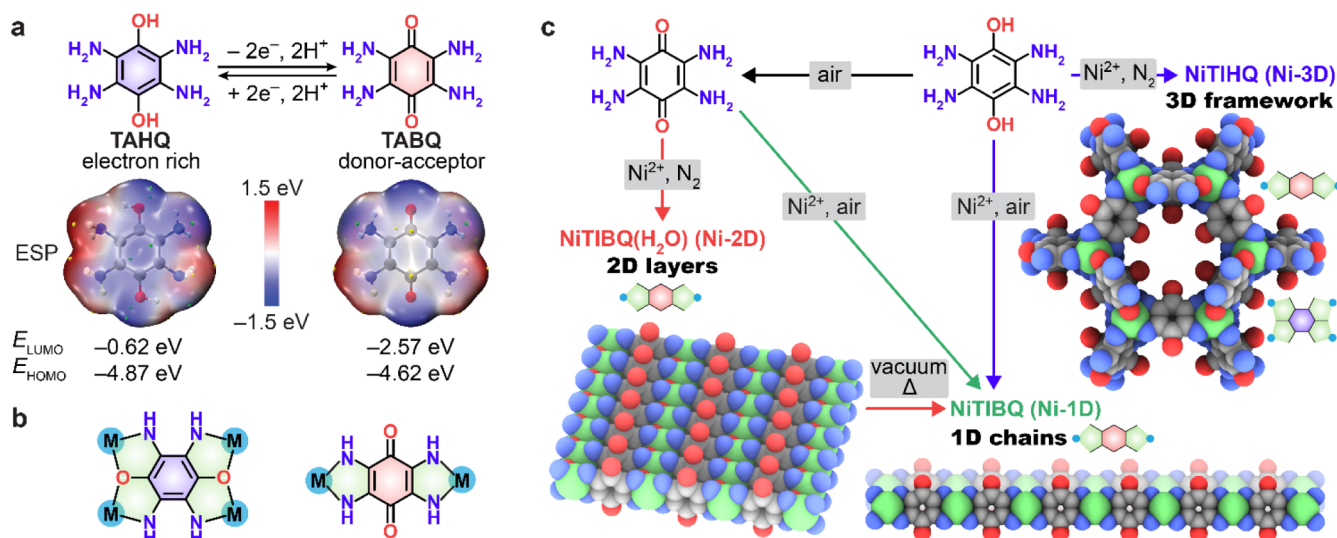


Figure 1. Ligand choice and synthetic conditions of Ni-based frameworks. (a) Chemical structures of TAHQ and TABQ with electrostatic potential (ESP) surfaces and HOMO and LUMO energies (at the B3LYP/def2-QZVP level). (b) Different connectivities of TAHQ (left) and TABQ (right) toward metals. (c) Schematic illustration of the synthetic details and transformation of Ni-1D, Ni-2D, and Ni-3D.

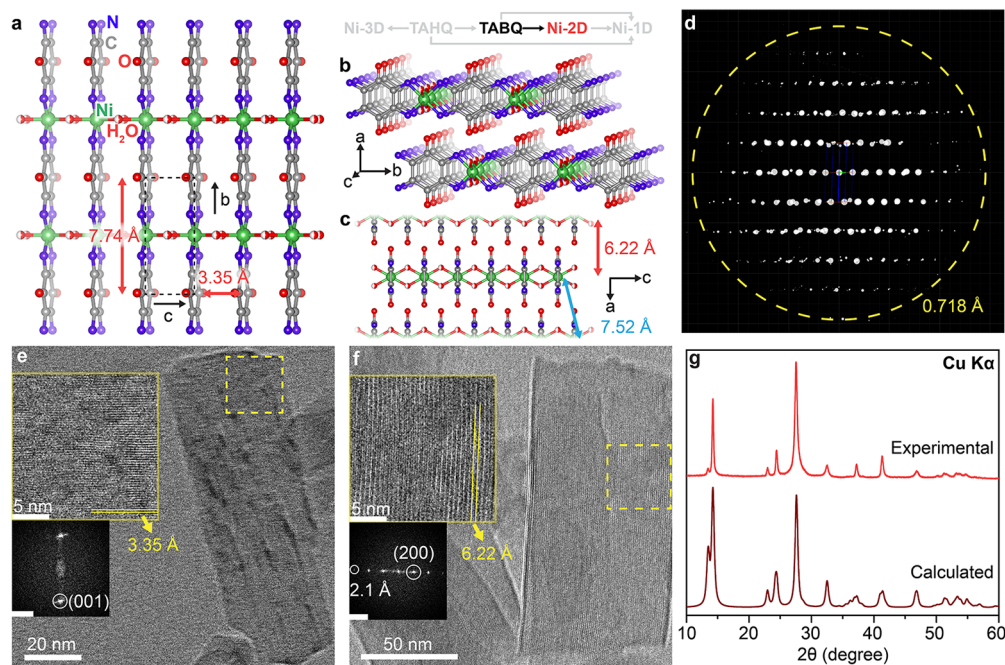


Figure 2. Structural characterizations of Ni-2D. (a) Part of a 2D layer of Ni-2D. Half-filled spheres represent the bridging H_2O molecules with 50% occupancy. Hydrogen atoms are omitted for clarity. The black dashed lines represent a unit cell. (b,c) Stacking of 2D layers. (d) 3D reciprocal lattices of a Ni-2D rod with a resolution down to 0.72 Å. (e) Cryo-EM image of a Ni-2D rod, showing the π - π stacking of TIBQ ligands within 2D layers across the whole rod. Upper and lower inset, the high-magnification image, and the FFT of the yellow dashed square. (f) Cryo-EM image of a Ni-2D rod, revealing interlayer stacking across the whole rod. Upper and lower inset, the high-magnification image, and the FFT of the yellow dashed square. Scale bars of FFTs, 2 nm^{-1} . (g) Experimental and calculated PXRD patterns of Ni-2D.

polymer chains, where it also functions to lower the band gap and promote charge transport.³¹

The electronic features of TAHQ and TABQ are best probed by UV-vis spectroscopy. A solution UV-vis spectrum of TABQ shows an intense intraquinone transition at 460 nm,^{32,33} with an absorption onset at 532 nm (Figure S3a). The optical gap is thus calculated to be 2.33 eV, close to the computed HOMO-LUMO gap of 2.05 eV. In comparison, the spectrum of TAHQ taken under an atmosphere of N_2 exhibits an absorption band for the hydroquinone π - π^* transition at 338 nm, whose onset gives

an optical gap of 3.45 eV.³⁴ Although the solution of TAHQ rapidly and completely oxidizes to TABQ within half an hour upon exposure to air, as evidenced by the evolution of the UV-vis spectra (Figure S3b), no isosbestic points are observed, suggesting that oxidation proceeds via an intermediate species.³⁵ A clue to this intermediate being the tetraamino-semiquinone radical comes from the growing and diminishing of a broad absorption at $\sim 850 \text{ nm}$ during the oxidation.³⁶ The D-A nature of TABQ is best revealed in the solid-state diffuse reflectance UV-vis spectrum (DRUV-vis, Figure S3c), which reveals a

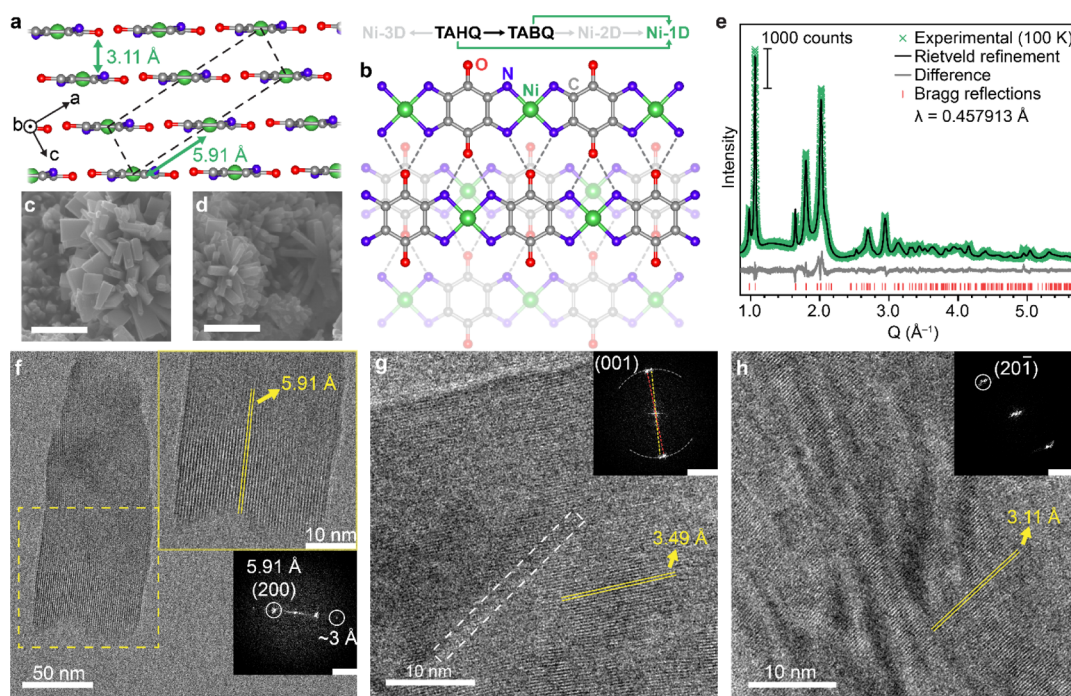


Figure 3. Structural characterizations of Ni-1D. (a) Interchain D–A π – π stacking of Ni-1D. Hydrogen atoms are omitted for clarity. The black dashed lines represent a unit cell. (b) Top-down view of the interchain D–A π – π stacking and interchain hydrogen bonding between –NH and C=O (gray dashed lines). (c,d) SEM images of Ni-1D microcrystals. Scale bars: 500 nm. (e) Rietveld refinement of the synchrotron PXRD pattern of Ni-1D, with $R_p = 4.17\%$, $R_{wp} = 5.34\%$, and $GoF = 1.39$. (f) Cryo-EM image of a single Ni-1D rod, showing TIBQ–Ni chains aligning along the a -axis. Upper and lower inset: high-magnification image and FFT of the yellow dashed square, respectively. (g) High magnification Cryo-EM image of a part of a Ni-1D rod, revealing TIBQ–Ni chains aligning along the c -axis. A grain boundary was highlighted by the white dashed rectangle. Inset: FFT of the micrograph. White dashed arcs indicate a Debye–Scherrer ring. Yellow and red dashed lines indicate two sets of diffraction spots. (h) High magnification Cryo-EM image of a part of a Ni-1D rod exhibiting interchain π – π stacking. Inset: FFT of the micrograph. Scale bars of FFTs: 2 nm^{-1} .

broad absorption from mid-visible to beyond 1000 nm. This feature is absent in the solution spectrum and is commonly associated with intermolecular charge transfer interactions. It gives an optical gap of 1.49 eV, significantly smaller than the solution value. UV–vis spectroscopy did not reveal any packing effects for TAHQ, whose spectra were qualitatively identical between solution and solid state.

Ni-Based Nonporous Frameworks. Solvothermal reaction between TABQ and $\text{Ni}(\text{OAc})_2 \cdot 4\text{H}_2\text{O}$ in degassed concentrated aqueous ammonia under an inert atmosphere at 120°C yields $\text{NiC}_6\text{H}_4\text{O}_3\text{N}_4$ ($\text{NiTIBQ}(\text{H}_2\text{O})$, Ni-2D) as a black microcrystalline powder consisting of rectangular rod-like crystals with lengths varying between 0.5 and $1.5 \mu\text{m}$ (Figure S4). The structure of Ni-2D was determined by continuous rotation electron diffraction (cRED) with an *ab initio* method.³⁷ The resolution of the cRED data sets was measured up to 0.72 \AA , allowing the location of all non-hydrogen atomic positions in Ni-2D with atomic precision (Figures 2d, S5, S6, and Table S2). The four amino groups in TABQ are deprotonated and chelate square-planar Ni^{2+} ions to form 1D chains of alternating tetraimino-benzoquinone (TIBQ) moieties and Ni^{2+} . The 1D chains are connected through bridging H_2O molecules to form 2D layers, where TIBQ moieties stack along the crystallographic c -axis in a fully eclipsed manner with a π – π stacking distance of $3.34(5) \text{ \AA}$ (Figure 2a,b). This distance is very close to the interlayer spacing of graphene sheets in graphite³⁸ and the interlayer spacing of highly conducting 2D MOFs.²⁶ The presence of bridging H_2O rather than OH^- or O^{2-} was further confirmed by O 1s X-ray photoelectron spectroscopy (XPS), which shows a characteristic water O 1s binding energy of 535.4

eV (Figure S8),^{39,40} and by attenuated total reflection (ATR)-FTIR, which reveals the characteristic water O–H stretching band at 3406 cm^{-1} (Figure S10 and related discussion therein).⁴¹ 2D layers of Ni-2D are staggered, likely due to the electrostatic repulsion of carbonyl O atoms, and crystallize in the orthorhombic space group *Immm* (Figure 2b,c), with the shortest interlayer Ni...Ni distance of 7.52 \AA .

The structural features of Ni-2D were also confirmed by high-resolution Cryo-EM down to a resolution of 2.1 \AA , which is prominent given the well-known beam sensitivity of similar hybrid materials.⁴² The Cryo-EM images showed that crystals of Ni-2D exhibit long-range ordering across the whole crystallite (Figures 2e,f and S11). Micrographs investigating the c crystallographic direction (Figures 2e and S11d) revealed the eclipsed π – π stacking of TIBQ–Ni chains within 2D layers of Ni-2D. A stacking distance of 3.35 \AA was obtained by analyzing the fast-Fourier transform (FFT, Figure 2e lower inset) of the highlighted area. Micrographs exploring the a crystallographic direction (Figures 2f and S11) showed 2D layers oriented parallel to the long side of the rod crystals with an interlayer spacing of 6.22 \AA . Altogether, the Cryo-EM data are in excellent agreement with the crystal structure derived from cRED. The excellent match between calculated and experimental powder X-ray diffraction (PXRD) patterns further confirmed the crystal structure and phase purity of the bulk material (Figure 2g).

Remarkably, repeating the synthetic conditions for Ni-2D in the presence of air produced $\text{NiC}_6\text{H}_4\text{O}_2\text{N}_4$ (NiTIBQ , Ni-1D), another black microcrystalline material that proved to be structurally distinct from Ni-2D.⁴³ Polycrystalline Ni-1D can also be synthesized from TAHQ·4HCl under aerobic conditions

(Figure S12) and consists of sharp-edged rectangular bricks and rods (Figures 3 and S13) up to 500 nm long. Because cRED caused electron beam damage in this case, the crystal structure of Ni-1D was solved by Rietveld refinement from high-resolution synchrotron PXRD data (Figure 3e).⁴⁴ As in Ni-2D, Ni-1D is formed from chains of TIBQ and Ni²⁺, formed by concomitant deprotonation and oxidation of TABQ or TAHQ under reaction conditions. The main structural difference between Ni-2D and Ni-1D is the absence of bridging water, which changes the packing of Ni-TIBQ chains from 2D layers in the former to brick-wall packing in the latter (Figure 3a).⁴⁵ This type of packing has been observed in organic semiconductors with high carrier mobility⁴⁶ and may be attributed here to interchain D–A interactions between partially oxidized TIBQ moieties (Figure 3b). The packing in Ni-1D leads to an interchain π – π stacking distance of 3.11 Å at 100 K, significantly shorter than that in Ni-2D, where bridging water molecules disrupt the D–A alignment. Notably, such close π – π stacking is rarely seen in conjugated metal–organic materials.⁴⁷ Interchain hydrogen bonding through –NH and C=O is also favorable given the appropriate alignment of chains (Figure 3b). The combination and balance between interchain D–A alignment and hydrogen bonding may also account for the two distinct morphologies observed in Ni-1D: parallelepipeds and rods, which can be explained by the Bravais–Friedel–Donnay–Harker (BFDH) law, and further verified by high-resolution Cryo-EM.

A micrograph of a Ni-1D single rod longer than 200 nm showed the long-range ordering of TIBQ–Ni chains across the whole crystallite down to a resolution of 3.0 Å, with an interchain spacing of 5.91 Å along the *a*-axis (Figure 3f). Cryo-EM also revealed the close packing enabled by D–A alignment along the *c* crystallographic direction, with an interchain spacing of ~3.5 Å (Figures 3g and S14d) and the close π – π stacking with a distance of ~3.1 Å (Figures 3h and S14d). Cryo-EM also revealed structural features that Rietveld refinement did not. Remarkably, a grain boundary formed by a subtle misalignment of the 1D chains was recognized by the presence of two sets of diffraction spots located on the same Debye–Scherrer ring with a misalignment angle of 5.8° (Figure 3g, inset). Grain boundaries can significantly affect charge transport in semiconductors and are often invoked, but have not yet been structurally resolved in conducting MOFs or CCPs.

Given the structural similarities between Ni-1D and Ni-2D, it is perhaps not surprising that the latter can transform into the former through the loss of bridging water. Albeit slowly, Ni-2D spontaneously transforms into Ni-1D over weeks under ambient conditions, suggesting that the D–A slipped π -stacking in Ni-1D is favorable energetically (Figure 4a). Lower temperature suppresses the transformation, whereas heating to 100 °C under dynamic vacuum considerably accelerates it (Figures 4b and S15). Continued heating of Ni-1D showed no further changes in its PXRD, attesting to its excellent thermal stability. The gradual removal of bridging water molecules was confirmed spectroscopically by ATR-FTIR (Figure S16), which revealed a gradual reduction in the intensity of the O–H stretching band for bridging water at 3406 cm⁻¹. The two N–H stretching bands of Ni-2D at 3297 and 3264 cm⁻¹ also merge into a single N–H band at 3245 cm⁻¹ that coincides with that observed for Ni-1D. Unlike Ni-2D, Ni-1D has good thermal stability and is also stable in strong acid [e.g., 4 M HCl (aq.)] and base [e.g., 1 M KOH (aq.)] (Figure S17), a rare feature in electrically conductive CCPs.³

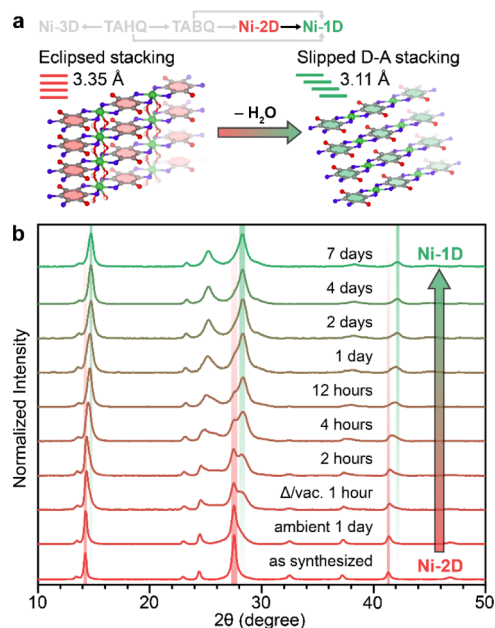


Figure 4. (a) Schematic representation and (b) *ex situ* PXRD patterns for the transformation from Ni-2D to Ni-1D.

Three-Dimensional, Porous Ni-TIHQ Framework. The reaction of TAHQ·4HCl with Ni(OAc)₂·4H₂O in degassed aqueous ammonia at 120 °C under a N₂ atmosphere yields brown hexagonal rodlike crystals of a Ni-TIHQ framework (Ni-3D) up to 40 μm long (Figures Sd inset, S18). Ni-3D undergoes a rapid color change from brown to black within half an hour of exposure to air (Figure S19), even though PXRD reveals no changes during this time (Figure S20). cRED analysis down to a resolution of 0.767 Å (Figures Sd, S21, S22, and Table S2) showed that crystals of oxidized Ni-3D (Ni₆C₆H₄O₂N₄, Ni-3D-ox) belong to the trigonal space group *R*3*m*. As with Ni-2D, the high-quality cRED data allowed for the direct location of all non-hydrogen atoms in Ni-3D-ox and revealed helical 1D rod secondary building units (SBUs) parallel to the *c*-axis (Figure 5b).⁴⁸ The SBUs consist of slightly distorted [NiN₄O₂] octahedra sharing two axial vertices and located on 3₁ screw axes (Figure 5b).

The SBUs are connected by TIHQ ligands into a hexagonal lattice (Figure 5a), where every Ni²⁺ is coordinated by two μ^4 -TIHQ and one μ^2 -TIHQ linkers. The μ^4 -TIHQ linkers use all six heteroatoms to chelate four independent Ni²⁺ ions from two adjacent SBUs, where each N atom binds to one Ni²⁺ and each O atom bridges two Ni²⁺ ions on the same SBU. This coordination mode is particularly notable because planar hexa-substituted triphenylenes and benzenes have thus far almost exclusively given rise to planar 2D MOFs with trigonal symmetry, with very few exceptions.^{49,50} The μ^2 -TIHQ linkers bridge two Ni²⁺ ions from two adjacent SBUs through four N atoms, similar to the coordination modes observed in Ni-1D and Ni-2D. Interestingly, the uncoordinated O atoms from μ^2 -TIHQ linkers point toward the center of the 1D hexagonal pores, leading to a highly hydrophilic pore environment (Figure 5a). Altogether, the overall topology of Ni-3D(-ox) is *fog* (Figure S23), and it is one of the two distinct (3,4)-*c* derived nets of the basic 4-*c nbo* net.⁵¹

In contrast to the dense nature of Ni-1D and Ni-2D (Figure S24a), Ni-3D-ox is intrinsically ultramicroporous with 1D pores with a diameter of ~4.2 Å, as indicated by the calculated Connolly surface (Figures 5c and S25). Upon activation, Ni-3D-

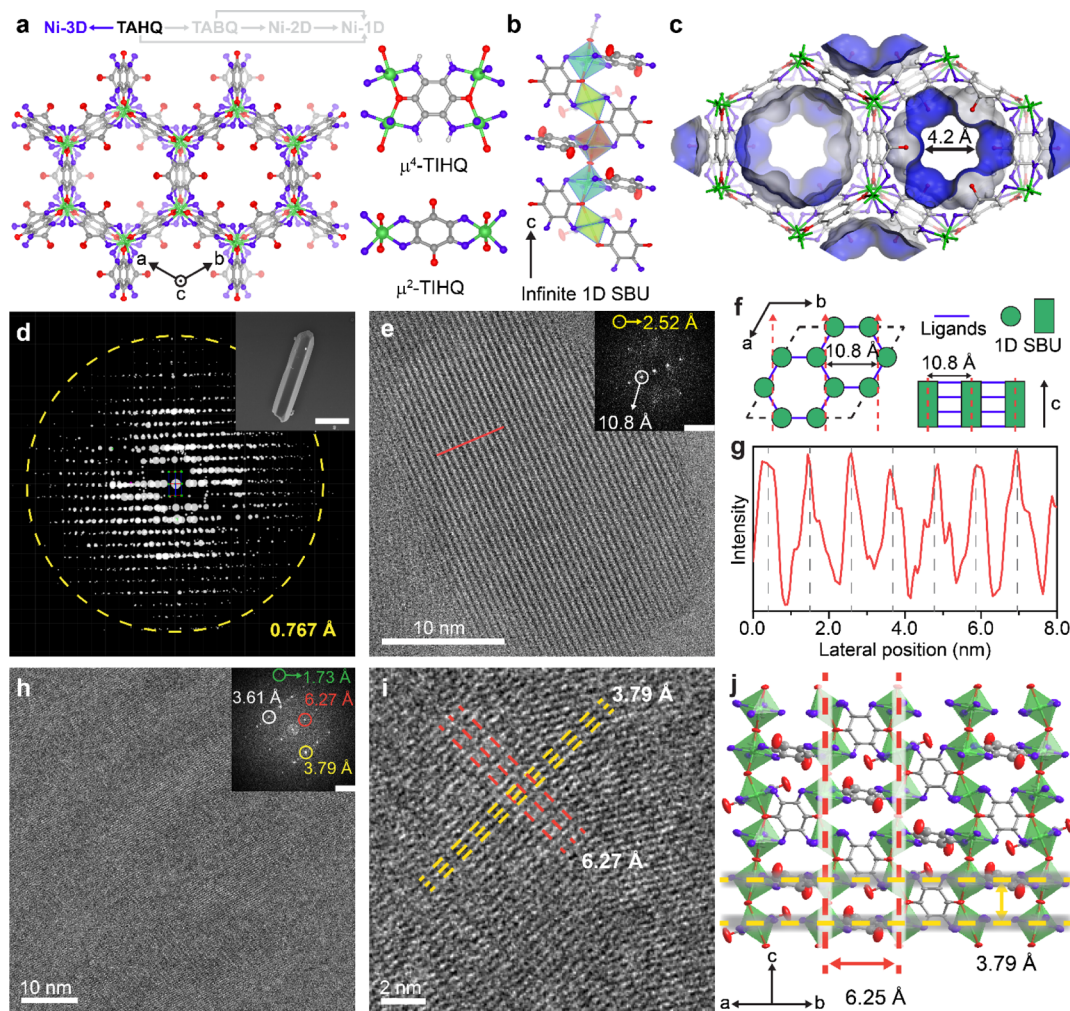


Figure 5. Structural characterization of Ni-3D-ox. (a) Portions of the crystal structure of Ni-3D-ox, built from octahedral $[\text{NiN}_4\text{O}_2]$ nodes, μ^4 -TIHQ linkers, and μ^2 -TIHQ linkers. (b) Portion of an infinite 1D rod SBU along the c crystallographic axis formed by octahedral $[\text{NiN}_4\text{O}_2]$ nodes through vertices sharing. (c) Connolly surface of a unit cell of Ni-3D-ox viewing along the c -axis. (d) 3D reciprocal lattices of a Ni-3D-ox rod with a maximum resolution of 0.77 Å. Inset: Single hexagonal rod of Ni-3D-ox. Scale bar: 5 μm . (e) High-magnification Cryo-EM image of a part of a Ni-3D-ox rod, showing well-aligned 1D SBUs. Inset: FFT of the micrograph. (f) Schematic representation of the Ni-3D-ox structure to illustrate the 1D SBUs alignment in (e). Red arrows and dashed lines indicate the viewing direction. (g) Intensity profile of the red solid line in (e), normal to the c -direction. Gray dashed lines with an even spacing of 10.9 Å are guides to the eye. (h) Cryo-EM image of a portion of a Ni-3D-ox single crystal. Inset: FFT of the micrograph. (i) High-magnification Cryo-EM image of the same crystal in (h), showing individual $[\text{NiN}_4\text{O}_2]$ nodes. Orthogonal yellow and red dashed lines indicate the packing of $[\text{NiN}_4\text{O}_2]$ nodes shown in (j). Scale bars for FFT: 2 nm^{-1} .

ox retains its crystallinity (Figures S18 and S20), and an N_2 adsorption isotherm at 77 K revealed a Brunauer–Emmett–Teller apparent surface area of $120 \text{ m}^2/\text{g}$ (Figure S24b). We note, however, that there is likely a substantial amount of H_2O that persists in the pores even after prolonged activation at 110°C (Figure S26) as suggested by the continued weight loss observed by thermogravimetric analysis upon heating from 100 to 300°C before eventual decomposition (Figure S27, Tables S3–S5). The persistent guest water molecules likely account for the lower apparent specific surface area relative to the theoretical value (Figure S25). In contrast, no significant weight loss was observed between 100 and 300°C for either Ni-1D or Ni-2D (Figures S28 and S29).

As with the previous materials, the structure of Ni-3D-ox was confirmed by near atomic-resolution Cryo-EM, down to 1.7 Å (Figure 5h). Long-range ordering of the SBUs was revealed by the evenly spaced high-contrast lattice fringes that align parallel to the c -axis (Figure 5e,f) with a spacing of 10.8 Å, confirmed by

both FFT (Figure 5e, inset) and line intensity profile normal to the c -axis (Figure 5g). Micrographs exploring the crystallographic orientation shown in Figure 5j exhibited highly ordered packing of $[\text{NiN}_4\text{O}_2]$ nodes across the whole crystal (Figures 5h and S30). Individual $[\text{NiN}_4\text{O}_2]$ octahedrons were clearly observed in the high-magnification micrograph of a portion of another Ni-3D-ox single crystal (Figure S30c), arranged as an orthogonal array with two average internode distances of 6.27 and 3.79 Å (Figure 5i), matched perfectly with the crystal structure solved by cRED. Bulk phase purity of Ni-3D-ox was verified by PXRD (Figure S31).

Assessing the Formal Oxidation States of the Ligands.

The physical and structural details of the three Ni materials are determined exclusively by the formal oxidation state of their linkers. Indeed, XPS confirmed that the Ni ions in all materials are divalent, with essentially identical Ni $2p_{3/2}$ binding energies (Figures S8, S9, S32).^{S2} A first indication of the degree of ligand oxidation came from comparing the C–C, C–O, and C–N

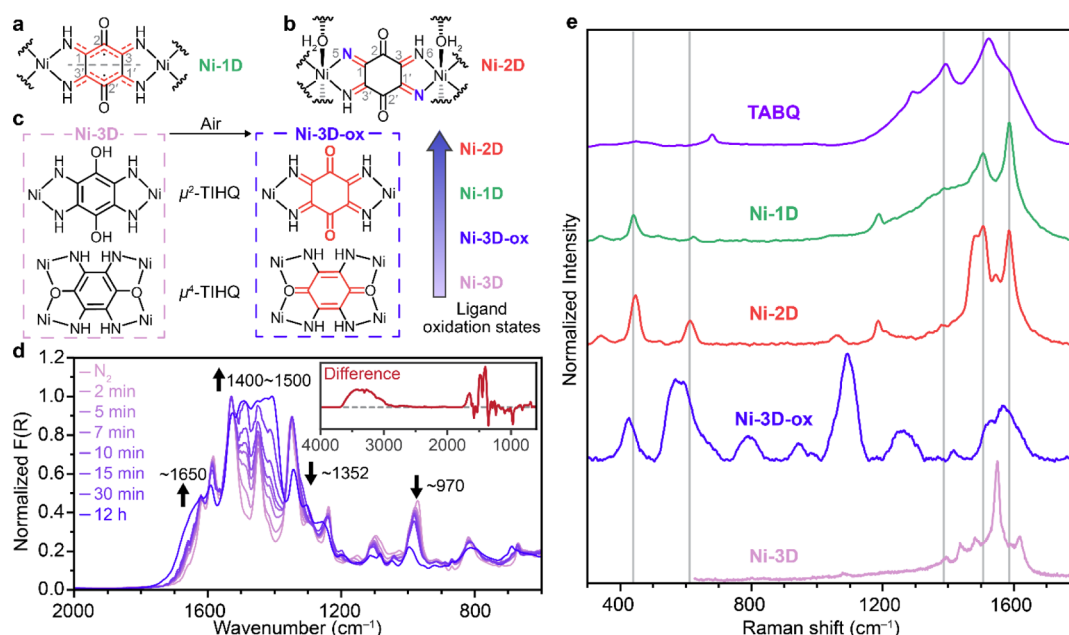


Figure 6. Characterization of ligand oxidation states. Lewis structures that can best describe (a) Ni-1D, (b) Ni-2D, (c) Ni-3D, and Ni-3D-ox. (d) *In situ* DRIFTS of Ni-3D upon exposure to air. Inset: the difference spectrum. (e) 532 nm Raman spectra of TABQ, Ni-1D, Ni-2D, Ni-3D-ox, and Ni-3D.

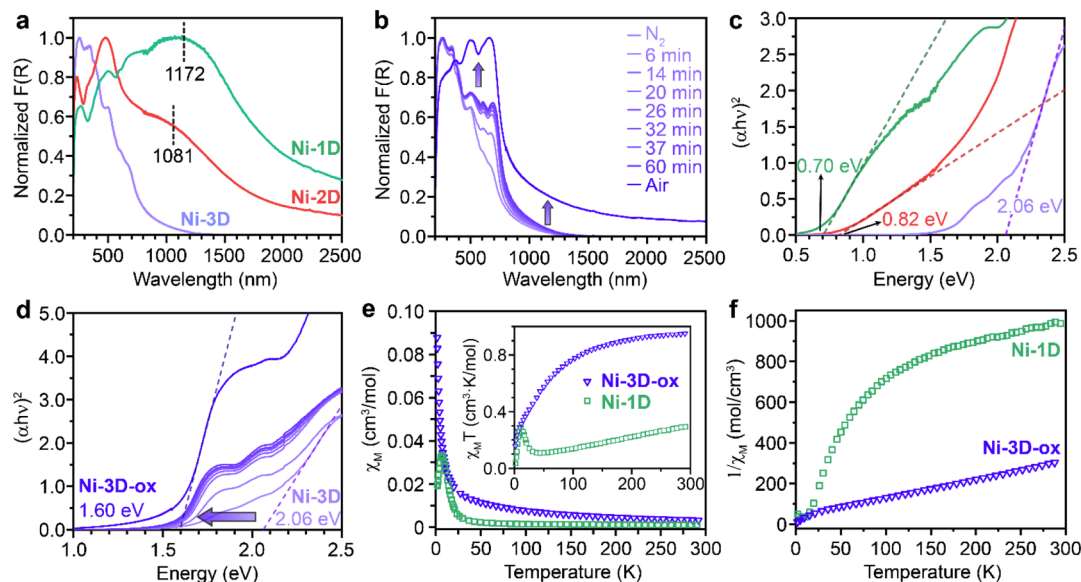


Figure 7. (a) Normalized DRUV-vis spectra and (c) Tauc plots of Ni-1D, Ni-2D, and Ni-3D. (b) *In situ* DRUV-vis spectra and (d) Tauc plots of Ni-3D upon exposure to air. Dashed lines indicate best linear fits to the absorption edges. (e, f) Temperature dependence of χ_M , $\chi_M T$, and χ_M^{-1} ($H = 1.0$ kOe) for Ni-1D and Ni-3D-ox.

bond lengths across the three materials. Because the TIBQ linkers in Ni-1D can be thought of as two N–C–C–N 5-center, 6π ($5c-6\pi$) subsystems, the C–C and C–N distances here are remarkably similar, 1.384 and 1.393 Å, respectively (Figure S33a). The 6π systems further function as a particularly effective electronic communication bridge between two Ni²⁺ centers. The two C–C bonds connecting the two 6π subsystems (C1–C3' and C1'–C3 in Figure 6a) show a more pronounced single bond character and an elongated bond distance of 1.454 Å, significantly longer than in the free ligand TABQ, 1.360 Å. Similar structural distortions have been observed in 2,5-diaminobenzoquinonediimine (DABQDI) metal complexes, such as planar Ni-DABQDI tapes,³² and oxidized TABQ

derivatives.⁵³ The C=O bond in Ni-1D is also slightly more extended to 1.261 Å relative to the free TABQ ligand's 1.237 Å, likely due to partial participation in the 6π subunit. In contrast, the C=O bond length in Ni-2D remains nearly unchanged compared to the free ligand's 1.232 Å, while the C–C distances undergo significant elongation to an average of 1.497 Å, closer to the single-bond character of C–C bonds in cyclohexane (1.53 Å) than the C–C bonds in aromatic rings (Figure S33c). The C–N bonds in Ni-2D show both C=NH and C=N[−] characters with an average C–N distance of 1.375 Å (Figure 6b). Altogether, the structural details point to a more oxidized form of TIBQ and a more localized electronic structure in Ni-2D than in Ni-1D.

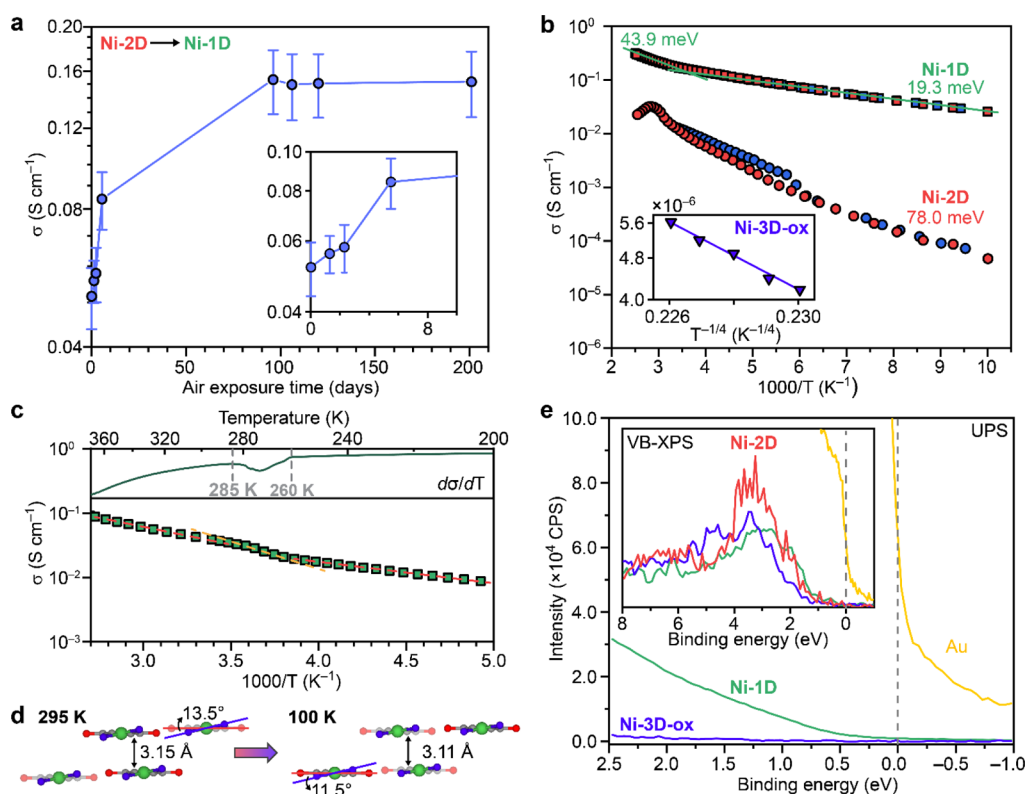


Figure 8. Electrical conductivity. (a) Conductivity increase during the transformation from Ni-2D to Ni-1D at ambient condition. Solid lines are a guide to the eye. (b) Temperature dependence of four-probe conductivities of Ni-1D, Ni-2D, and Ni-3D-ox. Red, heating; blue, cooling. Solid lines are the best linear fit. (c) Reversible E_A change of Ni-1D. Inset: the first derivative of electrical conductivity ($d\sigma/dT$). (d) Crystal structures of Ni-1D at 295 and 100 K. (e) Fermi edge region of UPS and VB-XPS. Gray dashed lines are the Fermi edge calibrated by sputtering-cleaned polycrystalline Au reference.

The color change accompanying the oxidation of Ni-3D to Ni-3D-ox likewise corresponds to the oxidation of TIHQ. Indeed, monitoring this rapid oxidation by *in situ* diffuse reflectance infrared Fourier transform spectroscopy (DRIFTS), showed gradually diminishing C–N and C–O stretching bands, and the concomitant growth of C=N and C=O stretching bands (Figure 6d). Thus, although TIHQ linkers in as-synthesized Ni-3D retain their hydroquinone character (Figure 6c), μ^2 -TIHQ and μ^4 -TIHQ in Ni-3D-ox are best described as being neutral and bearing a -4 negative charge, respectively, to give an overall neutral framework. Indeed, the C–O, C–C, and C–N distances and μ^4 -TIHQ in Ni-3D-ox are similar to that of free TABQ (which can be thought of as bearing a -4 charge balanced by 4 protons). Conversely, the C–O and C–N distances of 1.240 and 1.264 Å for μ^2 -TIHQ are typical for carbonyl C=O and imine C=NH moieties, respectively (Figure S33). Therefore, μ^2 -TIHQ linkers are best described as 1,2,4,5-tetraimino-3,6-diketocyclohexane (Figure 6c), a neutral ligand that has also been reported as such in a binuclear Ru complex.⁵⁴ Overall, the structural data reveal a redox ladder wherein the ligand is progressively oxidized in moving from Ni-3D to Ni-3D-ox, Ni-1D, and Ni-2D (Figure 6c).

The oxidation state of linkers was further confirmed by Raman spectroscopy, as the C–C, C–O, and C–N vibrational modes are highly sensitive to the ligand oxidation state.⁵⁵ The intense C=O stretching bands at ~ 1587 cm^{-1} for both Ni-1D and Ni-2D are slightly red-shifted relative to TABQ at 1595 cm^{-1} (Figures 6e and S34 and related discussion therein). The broad C–N stretching band at 1387 cm^{-1} observed for Ni-1D can be explained by the highly delocalized nature of the 6π

subsystems.⁵⁶ In comparison, the two bands at 1506 and 1547 cm^{-1} observed for Ni-2D, corresponding to C=NH and C=N[−] stretching modes, attest to the more oxidized ligand in this material.⁵⁶ Notably, benzene ring breathing bands at 1619 and 1551 cm^{-1} for Ni-3D shift and merge into a new C–C stretching band at 1531 cm^{-1} upon formation of Ni-3D-ox, confirming the oxidation of TIHQ linkers (Figures 6e and S35). The Raman bands between 400 and 650 cm^{-1} in all spectra correspond to Ni–N and/or Ni–O bonds.

Electronic Structures. Initial assessment for the degree of charge delocalization and metal–ligand conjugation in the three Ni frameworks came from electronic structure investigations by DRUV-vis and magnetometry. Both Ni-1D and Ni-2D exhibit strong electronic absorptions around 500 nm, corresponding to ligand-centered (LC) π – π^* intraquinone excitations (Figures 7a and S36).^{32,33} The absorption maximum of Ni-1D, 503 nm, is slightly red-shifted compared to Ni-2D, 475 nm, consistent with the higher degree of delocalization in the former. In contrast, Ni-3D shows a hydroquinone-based LC π – π^* transition at 344 nm.³⁴ Broad metal-to-ligand charge transfer (MLCT) bands centered around 750 nm and 732 nm were observed for Ni-1D and Ni-2D,³² respectively. These absorption bands are significantly red-shifted compared with those in related 2,5-diamino-1,4-diiminobenzoquinone complexes^{57–59} and indicate significant electronic delocalization between Ni²⁺ and TIBQ orbitals. The two broad NIR bands, centered at 1172 nm for Ni-1D and 1081 nm for Ni-2D, stem from extended intrachain metal–ligand d – π conjugation and strong interchain stacking. In contrast, Ni-3D exhibits essentially no MLCT features or NIR bands, which suggests that it lacks intrinsic

charge delocalization. However, oxidation to Ni-3D-ox coincides with the gradual growth of MLCT bands centered around 506 and 660 nm (Figure 7b), suggesting substantially enhanced metal–ligand electronic communication with oxidation of TIHQ. Although the NIR region in Ni-3D-ox gains intensity relative to Ni-3D, indicating the increase of free carrier concentration and electronic delocalization,⁶⁰ it is still much weaker than the NIR features of Ni-2D and Ni-1D. Extracting optical band gaps (E_g) from the DRUV-vis spectra by the way of Tauc plots revealed decreasing values of 2.06, 1.60, 0.82, and 0.70 eV for Ni-3D, Ni-3D-ox, Ni-2D, and Ni-1D, respectively (Figure 7c,d).

Magnetometry provided critical insights into the electronic communication between metals and/or ligands. Direct current (DC) magnetic susceptibilities were measured for polycrystalline samples of Ni-1D and Ni-3D-ox⁶¹ from 1.8 to 293 K under an applied field of 1 kOe (Figure 7e). Ni-1D has $\chi_M T$ of 0.30 cm³ K mol⁻¹ per Ni-TIBQ unit at 293 K, much lower than the value of 1 cm³ K mol⁻¹ expected for high-spin Ni²⁺ centers with $S = 1$. $\chi_M T$ for Ni-1D gradually decreases with decreasing temperature, but sees a sharp increase between 45 and 11 K. This behavior is consistent with the presence of both ferromagnetic and antiferromagnetic exchange pathways. For structurally closely related molecular analogues, such as Ni(isq)₂ (isq = *o*-diiminobenzosemiquinonate) complexes,^{62,63} square-planar Ni²⁺ ions typically exhibit closed-shell $S = 0$ configurations. Therefore, the antiferromagnetic coupling here likely arises from the Ni-mediated interaction between TIBQ-centered radicals (Figure S37), again in close analogy to the Ni(isq)₂ complexes.⁶⁴

Ni-3D-ox exhibits a $\chi_M T$ value of 0.95 cm³ K mol⁻¹ per Ni-TIHQ unit at 293 K, very close to the value expected for a Ni²⁺-centered $S = 1$ spin and a closed-shell TIHQ linker (1 cm³ K mol⁻¹ for $g = 2.0$). The $\chi_M T$ value gradually decreases to 0.158 cm³ K mol⁻¹ at 1.8 K, suggesting an overall antiferromagnetic coupling between the Ni-centered spins. Fitting the χ_M^{-1} versus T curve in the high-temperature region to the Curie–Weiss law gives a Curie constant C of 1.04 cm³ K mol⁻¹ and a Weiss temperature $\theta = -25.4$ K (Figures 7f and S38). In contrast to Ni-1D, Ni-3D-ox can be described as a network of isolated $S = 1$ spins centered on Ni²⁺, coupled by weak antiferromagnetic interactions. The weak antiferromagnetic coupling observed here further points to the absence of TIHQ-centered radicals, whose presence would have enabled strong exchange coupling with Ni-centered spin systems by analogy with molecular complexes.^{36,65} The presence of organic radicals in Ni-1D and Ni-2D and the absence thereof in Ni-3D-ox was confirmed by electron paramagnetic resonance (EPR) spectroscopy. The characteristic signal at $g = 2.05$ and 2.08 observed for Ni-1D and Ni-2D, respectively, is ~ 200 times weaker in Ni-3D-ox (Figure S39).

Electrical Conductivity. The distinct electronic structures of Ni-1D, Ni-2D, and Ni-3D(-ox) give rise to electrical conductivities that span almost 8 orders of magnitude, from 10⁻⁹ S cm⁻¹ to nearly 1 S cm⁻¹. Four-contact probe measurements of polycrystalline pellets of Ni-1D and Ni-2D revealed bulk electrical conductivities reaching 0.19 S cm⁻¹ ($\bar{\sigma} = (0.16 \pm 0.02)$ S cm⁻¹) and 0.067 S cm⁻¹ ($\bar{\sigma} = (0.054 \pm 0.009)$ S cm⁻¹), respectively, at room temperature (RT), which are on par with the most conductive 1D CCPs to date.³ Interestingly, the conductivity of Ni-1D increased by about 60% to 0.27 S cm⁻¹ after treatment with HCl (Figures S40 and S41), similar to the p-doping of polyaniline. The transformation of Ni-2D to Ni-1D at RT over the course of several (Covid-induced lockdown)

months coincided with a gradual increase in electrical conductivity (Figures 8a and S42–S45). Given the similar crystallite size and the same metal–ligand connectivity in these two materials, we attribute the higher electrical conductivity of Ni-1D to its interchain D–A stacking and shorter π – π stacking distance.

Under anaerobic conditions, Ni-3D exhibits a two-probe electrical conductivity of 6.2 $\times 10^{-9}$ S cm⁻¹, as may be expected in the absence of π – π stacking and weak covalency of the metal–ligand bond.^{1,2} Upon exposure to air, the conductivity increases to 6.7 $\times 10^{-7}$ S cm⁻¹ after 12 h to finally reach a maximum conductivity of 2.9 $\times 10^{-5}$ S cm⁻¹ for Ni-3D-ox, a remarkable value for 3D-connected, porous MOFs.⁶⁶ The increase in conductivity in going from Ni-3D to Ni-3D-ox is paralleled by a substantial decrease of ~ 0.5 eV for E_g . This implies that increasing the ligand oxidation state modifies the electronic structure of the framework, which translates to improved charge transport.

Variable-temperature conductivity measurements revealed semiconducting behavior for all three materials (Figure 8b). Ni-1D and Ni-2D exhibit Arrhenius-type dependence of the conductivity with temperature T

$$\sigma_{e,T} = \sigma_{e,\infty} \exp\left(-\frac{E_A}{k_B T}\right)$$

where $\sigma_{e,\infty}$ is the temperature-independent prefactor and E_A is the thermal activation energy. This behavior is typical for doped organic semiconductors and conductive MOFs with band-like charge transport.^{1,2,67}

A notable increase in E_A for Ni-1D from 19.3 meV at $T < \sim 260$ K to 43.9 meV at $T > \sim 285$ K (Figures 8c and S46) is correlated with a reversible structural change that occurs at approximately 270 K (Figures 8c and S47). Indeed, Rietveld refinement of synchrotron PXRD data for Ni-1D at 295 K (Figure S48) revealed a longer interchain π – π stacking distance of 3.15 Å (3.11 Å at 100 K) and a larger dihedral angle of 13.5° between the six-membered carbon ring and five-membered Ni chelating ring (11.5° at 100 K) (Figure 8d), suggesting that the interchain and intrachain transport are both weakened, in agreement with the higher E_A .

Ni-2D showed a significantly higher E_A of 78.0 meV in the temperature range 100–300 K (Figure 8b). The apparent decrease in conductivity above 60 °C is *not* an indication of a transition to a temperature-deactivated transport. Rather, we attribute it to the partial transformation of Ni-2D to Ni-1D; the associated disorder accompanying this transformation is the more likely cause of the decreasing electrical conductivity with temperature (Figure S49). For context, these E_A values are still smaller than those observed for heavily *n*-doped C₆₀, one of the most conductive doped organic semiconductors, and suggest exceptional electronic coupling and small energetic disorder in our materials.⁶⁷

In contrast to the lower dimensionality structures, Ni-3D-ox shows variable-range hopping (VRH) transport, which is best described by Mott's VRH theory (Figures 8b inset, S50)⁶⁸

$$\sigma_{e,T} = \sigma_{e,0} \exp\left[-\left(\frac{T_0}{T}\right)^{1/d+1}\right]$$

where d is the dimensionality of transport ($d = 3$ for Ni-3D-ox), $\sigma_{e,0}$ is the temperature-independent constant and equals the $T \rightarrow \infty$ value of $\sigma_{e,T}$, and T_0 is the Mott temperature. The latter is

related to the charge-carrier concentration and carrier hopping length between adjacent localized states. We believe that the increased conductivity of Ni-3D-ox relative to Ni-3D is due to ligand oxidation, which generates charge carriers and localized sites that overall decrease the hopping distance. We note that VRH theory also fits the variable temperature conductivity data for Ni-2D (with $d = 2$), indicating that the charge transport in this material occurs primarily within the 2D layers and that interlayer electronic interactions are weak (Figure S51).

Valence-band XPS (VB-XPS) and ultraviolet photoelectron spectroscopy (UPS) corroborate the electronic structure insights afforded by conductivity measurements. The highest occupied states (HOS) of Ni-1D and Ni-3D-ox revealed by UPS are ~ 0.45 and ~ 1.3 eV below the Fermi level E_F (Figures 8e and S52), respectively. Fitting of the VB-XPS edge gives a higher HOS level for Ni-1D, which is only about ~ 0.2 eV below E_F , indicating the substantial contribution of Ni orbitals to the density of states (DOS) near the valence band maximum (VBM) and the close match of ligand and metal energy levels (Figure S53). The shallow HOS below E_F of Ni-1D is consistent with its high electrical conductivity. Ni-2D exhibits moderate HOS (~ 0.6 eV below E_F), again in good agreement with its slightly lower conductivity relative to Ni-1D.

CONCLUSIONS AND OUTLOOK

Despite the considerable interest in the electronic properties of MOFs and coordination polymers, it has been difficult to design systems that enable correlations between physical properties and structure. Indeed, when structure–function relationships are discussed in this context, changes in the structure usually are also accompanied or caused by compositional changes.^{69–71} Here, we showed that owing to their multiple redox states and metal binding preference, the redox series comprising TAHQ, TABQ, and TIBQ provides a unique platform to study structure–function relationships in essentially isomeric Ni MOFs/coordination polymers. These results thus provide important insights into how dimensionality and various supramolecular interactions between SBUs, ligands, and structural motifs (i.e., D–A, hydrogen bonding, and π – π stacking) lead to differences of nearly 8 orders of magnitude in electrical conductivity. Ligands that combine a similar breadth of redox states and metal-chelating motifs should provide inspiration for future material design.

ASSOCIATED CONTENT

Supporting Information

The Supporting Information is available free of charge at <https://pubs.acs.org/doi/10.1021/jacs.2c00614>.

Computational methods, electron diffraction micrographs, SEM, TEM, PXRD patterns, electronic and vibrational spectra, EPR, magnetism, I – V curves, and photoelectron spectra (PDF)

Accession Codes

CCDC 2121221–2121222 contain the supplementary crystallographic data for this paper. These data can be obtained free of charge via www.ccdc.cam.ac.uk/data_request/cif, or by emailing data_request@ccdc.cam.ac.uk, or by contacting The Cambridge Crystallographic Data Centre, 12 Union Road, Cambridge CB2 1EZ, UK; fax: +44 1223 336033.

AUTHOR INFORMATION

Corresponding Authors

Jian Li – Berzelii Center EXSELENT on Porous Materials, Department of Materials and Environmental Chemistry, Stockholm University, Stockholm 10691, Sweden; Department of Fibre and Polymer Technology, KTH Royal Institute of Technology, Stockholm 10044, Sweden; Email: jian5@kth.se
Mircea Dincă – Department of Chemistry, Massachusetts Institute of Technology, Cambridge, Massachusetts 02139, United States; orcid.org/0000-0002-1262-1264; Email: mdinca@mit.edu

Authors

Tianyang Chen – Department of Chemistry, Massachusetts Institute of Technology, Cambridge, Massachusetts 02139, United States; orcid.org/0000-0003-3142-8176
Jin-Hu Dou – Department of Chemistry, Massachusetts Institute of Technology, Cambridge, Massachusetts 02139, United States; orcid.org/0000-0002-6920-9051
Luming Yang – Department of Chemistry, Massachusetts Institute of Technology, Cambridge, Massachusetts 02139, United States
Chenyue Sun – Department of Chemistry, Massachusetts Institute of Technology, Cambridge, Massachusetts 02139, United States
Julius J. Oppenheim – Department of Chemistry, Massachusetts Institute of Technology, Cambridge, Massachusetts 02139, United States

Complete contact information is available at: <https://pubs.acs.org/10.1021/jacs.2c00614>

Notes

The authors declare no competing financial interest.

ACKNOWLEDGMENTS

This work was supported by the Army Research Office (award no. W911NF-21-1-0124). Part of this work (SEM, part of XPS, and Raman) made use of the MRSEC Shared Experimental Facilities at MIT, supported by the National Science Foundation under award no. 1419807, and the Harvard Center for Nanoscale Systems (CNS), supported by the National Science Foundation under award no. 1541959. The cRED data were collected at the Electron Microscopy Center (EMC) in Stockholm University with the support of the Knut and Alice Wallenberg Foundation (KAW, 2012-0112) through the 3DEM-NATUR project. Cryo-EM specimens were prepared and imaged at the Automated Cryogenic Electron Microscopy Facility in MIT.nano on a Talos Arctica microscope, a gift from the Arnold and Mabel Beckman Foundation. Use of the Advanced Photon Source at Argonne National Laboratory was supported by the U. S. Department of Energy under contract no. DE-AC02-06CH11357. We thank Dr. Edward Brignole for help with Cryo-EM and Dr. Grigorii Skorupskii for help with Rietveld refinement.

REFERENCES

- (1) Sun, L.; Campbell, M. G.; Dincă, M. Electrically Conductive Porous Metal–Organic Frameworks. *Angew. Chem., Int. Ed.* **2016**, *55*, 3566–3579.
- (2) Xie, L. S.; Skorupskii, G.; Dincă, M. Electrically Conductive Metal–Organic Frameworks. *Chem. Rev.* **2020**, *120*, 8536–8580.

- (3) Givaja, G.; Amo-Ochoa, P.; Gómez-García, C. J.; Zamora, F. Electrical Conductive Coordination Polymers. *Chem. Soc. Rev.* **2012**, *41*, 115–147.
- (4) Huang, X.; Sheng, P.; Tu, Z.; Zhang, F.; Wang, J.; Geng, H.; Zou, Y.; Di, C.-A.; Yi, Y.; Sun, Y.; Xu, W.; Zhu, D. A Two-Dimensional π -d Conjugated Coordination Polymer with Extremely High Electrical Conductivity and Ambipolar Transport Behaviour. *Nat. Commun.* **2015**, *6*, 7408.
- (5) Sheberla, D.; Bachman, J. C.; Elias, J. S.; Sun, C.-J.; Shao-Horn, Y.; Dincă, M. Conductive MOF Electrodes for Stable Supercapacitors with High Areal Capacitance. *Nat. Mater.* **2017**, *16*, 220–224.
- (6) Feng, D.; Lei, T.; Lukatskaya, M. R.; Park, J.; Huang, Z.; Lee, M.; Shaw, L.; Chen, S.; Yakovenko, A. A.; Kulkarni, A.; Xiao, J.; Fredrickson, K.; Tok, J. B.; Zou, X.; Cui, Y.; Bao, Z. Robust and Conductive Two-Dimensional Metal–Organic Frameworks with Exceptionally High Volumetric and Areal Capacitance. *Nat. Energy* **2018**, *3*, 30–36.
- (7) Banda, H.; Dou, J.-H.; Chen, T.; Libretto, N. J.; Chaudhary, M.; Bernard, G. M.; Miller, J. T.; Michaelis, V. K.; Dincă, M. High-Capacitance Pseudocapacitors from Li^+ Ion Intercalation in Nonporous, Electrically Conductive 2D Coordination Polymers. *J. Am. Chem. Soc.* **2021**, *143*, 2285–2292.
- (8) Wang, K.-B.; Xun, Q.; Zhang, Q. Recent Progress in Metal–Organic Frameworks as Active Materials for Supercapacitors. *EnergyChem* **2020**, *2*, 100025.
- (9) Shinde, S. S.; Lee, C. H.; Jung, J.-Y.; Wagh, N. K.; Kim, S.-H.; Kim, D.-H.; Lin, C.; Lee, S. U.; Lee, J.-H. Unveiling Dual-Linkage 3D Hexaiminobenzene Metal–Organic Frameworks towards Long-Lasting Advanced Reversible Zn–Air Batteries. *Energy Environ. Sci.* **2019**, *12*, 727–738.
- (10) Nam, K. W.; Park, S. S.; dos Reis, R.; Dravid, V. P.; Kim, H.; Mirkin, C. A.; Stoddart, J. F. Conductive 2D Metal–Organic Framework for High-Performance Cathodes in Aqueous Rechargeable Zinc Batteries. *Nat. Commun.* **2019**, *10*, 4948.
- (11) Wu, Z.; Adekoya, D.; Huang, X.; Kiefel, M. J.; Xie, J.; Xu, W.; Zhang, Q.; Zhu, D.; Zhang, S. Highly Conductive Two-Dimensional Metal–Organic Frameworks for Resilient Lithium Storage with Superb Rate Capability. *ACS Nano* **2020**, *14*, 12016–12026.
- (12) Wu, Z.; Xie, J.; Xu, Z. J.; Zhang, S.; Zhang, Q. Recent Progress in Metal–Organic Polymers as Promising Electrodes for Lithium/Sodium Rechargeable Batteries. *J. Mater. Chem. A* **2019**, *7*, 4259–4290.
- (13) Clough, A. J.; Yoo, J. W.; Mecklenburg, M. H.; Marinescu, S. C. Two-Dimensional Metal–Organic Surfaces for Efficient Hydrogen Evolution from Water. *J. Am. Chem. Soc.* **2015**, *137*, 118–121.
- (14) Miner, E. M.; Fukushima, T.; Sheberla, D.; Sun, L.; Surendranath, Y.; Dincă, M. Electrochemical Oxygen Reduction Catalysed by $\text{Ni}_3(\text{Hexaiminotriphenylene})_2$. *Nat. Commun.* **2016**, *7*, 10942.
- (15) Miner, E. M.; Wang, L.; Dincă, M. Modular O_2 Electroreduction Activity in Triphenylene-Based Metal–Organic Frameworks. *Chem. Sci.* **2018**, *9*, 6286–6291.
- (16) Campbell, M. G.; Sheberla, D.; Liu, S. F.; Swager, T. M.; Dincă, M. $\text{Cu}_3(\text{Hexaiminotriphenylene})_2$: An Electrically Conductive 2D Metal–Organic Framework for Chemiresistive Sensing. *Angew. Chem., Int. Ed.* **2015**, *54*, 4349–4352.
- (17) Campbell, M. G.; Liu, S. F.; Swager, T. M.; Dincă, M. Chemiresistive Sensor Arrays from Conductive 2D Metal–Organic Frameworks. *J. Am. Chem. Soc.* **2015**, *137*, 13780–13783.
- (18) Stassen, I.; Dou, J.-H.; Hendon, C.; Dincă, M. Chemiresistive Sensing of Ambient CO_2 by an Autogenously Hydrated $\text{Cu}_3(\text{Hexaiminobenzene})_2$ Framework. *ACS Cent. Sci.* **2019**, *5*, 1425–1431.
- (19) Sun, L.; Liao, B.; Sheberla, D.; Kraemer, D.; Zhou, J.; Stach, E. A.; Zakharov, D.; Stavila, V.; Talin, A. A.; Ge, Y.; Allendorf, M. D.; Chen, G.; Léonard, F.; Dincă, M. A Microporous and Naturally Nanostructured Thermoelectric Metal–Organic Framework with Ultralow Thermal Conductivity. *Joule* **2017**, *1*, 168–177.
- (20) Erickson, K. J.; Léonard, F.; Stavila, V.; Foster, M. E.; Spataru, C. D.; Jones, R. E.; Foley, B. M.; Hopkins, P. E.; Allendorf, M. D.; Talin, A. A. Thin Film Thermoelectric Metal–Organic Framework with High Seebeck Coefficient and Low Thermal Conductivity. *Adv. Mater.* **2015**, *27*, 3453–3459.
- (21) Huang, X.; Zhang, S.; Liu, L.; Yu, L.; Chen, G.; Xu, W.; Zhu, D. Superconductivity in a Copper(II)-Based Coordination Polymer with Perfect Kagome Structure. *Angew. Chem., Int. Ed.* **2018**, *57*, 146–150.
- (22) Takenaka, T.; Ishihara, K.; Roppongi, M.; Miao, Y.; Mizukami, Y.; Makita, T.; Tsurumi, J.; Watanabe, S.; Takeya, J.; Yamashita, M.; Torizuka, K.; Uwatoko, Y.; Sasaki, T.; Huang, X.; Xu, W.; Zhu, D.; Su, N.; Cheng, J. G.; Shibauchi, T.; Hashimoto, K. Strongly Correlated Superconductivity in a Copper-Based Metal–Organic Framework with a Perfect Kagome Lattice. *Sci. Adv.* **2021**, *7*, No. eabf3996.
- (23) Sheberla, D.; Sun, L.; Blood-forsythe, M. A.; Er, S.; Wade, C. R.; Brozek, C. K.; Aspuru-Guzik, A.; Dincă, M. High Electrical Conductivity in $\text{Ni}_3(2,3,6,7,10,11\text{-Hexaiminotriphenylene})_2$, a Semiconducting Metal–Organic Graphene Analogue. *J. Am. Chem. Soc.* **2014**, *136*, 8859–8862.
- (24) Day, R. W.; Bediako, D. K.; Rezaee, M.; Parent, L. R.; Skorupskii, G.; Arguilla, M. Q.; Hendon, C. H.; Stassen, I.; Gianneschi, N. C.; Kim, P.; Dincă, M. Single Crystals of Electrically Conductive Two-Dimensional Metal–Organic Frameworks: Structural and Electrical Transport Properties. *ACS Cent. Sci.* **2019**, *5*, 1959–1964.
- (25) Park, J.; Hincley, A. C.; Huang, Z.; Feng, D.; Yakovenko, A. A.; Lee, M.; Chen, S.; Zou, X.; Bao, Z. Synthetic Routes for a 2D Semiconductive Copper Hexahydroxybenzene Metal–Organic Framework. *J. Am. Chem. Soc.* **2018**, *140*, 14533–14537.
- (26) Chen, T.; Dou, J.-H.; Yang, L.; Sun, C.; Libretto, N. J.; Skorupskii, G.; Miller, J. T.; Dincă, M. Continuous Electrical Conductivity Variation in $\text{M}_3(\text{Hexaiminotriphenylene})_2$ ($\text{M} = \text{Co}, \text{Ni}, \text{Cu}$) MOF Alloys. *J. Am. Chem. Soc.* **2020**, *142*, 12367–12373.
- (27) Meng, Z.; Luo, J.; Li, W.; Mirica, K. A. Hierarchical Tuning of the Performance of Electrochemical Carbon Dioxide Reduction Using Conductive Two-Dimensional Metallophthalocyanine Based Metal–Organic Frameworks. *J. Am. Chem. Soc.* **2020**, *142*, 21656–21669.
- (28) Dou, J.-H.; Sun, L.; Ge, Y.; Li, W.; Hendon, C. H.; Li, J.; Gul, S.; Yano, J.; Stach, E. A.; Dincă, M. Signature of Metallic Behavior in the Metal–Organic Frameworks $\text{M}_3(\text{Hexaiminobenzene})_2$ ($\text{M} = \text{Ni}, \text{Cu}$). *J. Am. Chem. Soc.* **2017**, *139*, 13608–13611.
- (29) Lu, T.; Chen, F. Multiwfn: A Multifunctional Wavefunction Analyzer. *J. Comput. Chem.* **2012**, *33*, 580–592.
- (30) Sato, M.; Takeda, T.; Hoshino, N.; Akutagawa, T. Electronic and Crystal Structures of 1,2,3-Triazole-Fused p-Benzoquinone Derivatives. *CrystEngComm* **2017**, *19*, 910–917.
- (31) Müllen, K.; Pisula, W. Donor–Acceptor Polymers. *J. Am. Chem. Soc.* **2015**, *137*, 9503–9505.
- (32) Audi, H.; Chen, Z.; Charaf-Eddin, A.; D’Aléo, A.; Canard, G.; Jacquemin, D.; Siri, O. Extendable Nickel Complex Tapes That Reach NIR Absorptions. *Chem. Commun.* **2014**, *50*, 15140–15143.
- (33) Rall, J.; Stange, A. F.; Hübler, K.; Kaim, W. A Coordination-Induced 1,4→1,2-Quinonediiimine Isomerization. *Angew. Chem., Int. Ed.* **1998**, *37*, 2681–2682.
- (34) Yamamoto, T.; Kimura, T.; Shirashi, K. Preparation of π -Conjugated Polymers Composed of Hydroquinone, p-Benzoquinone, and p-Diacetoxyphenylene Units. Optical and Redox Properties of the Polymers. *Macromolecules* **1999**, *32*, 8886–8896.
- (35) Metcalfe, R. A.; Vasconcellos, L. C. G.; Mirza, H.; Franco, D. W.; Lever, A. B. P. Synthesis and Characterization of Dinuclear Complexes of 3,3',4,4'-Tetraminobiphenyl with Tetramminoruthenium and Bis-(bipyridine)ruthenium Residues and Their Two- and Four-Electron Oxidized Products Including a ZINDO Study of Orbital Mixing as a Function of Ligand Oxidation State. *J. Chem. Soc., Dalton Trans.* **1999**, *16*, 2653–2667.
- (36) Chakarawet, K.; Harris, T. D.; Long, J. R. Semiquinone Radical-Bridged M_2 ($\text{M} = \text{Fe}, \text{Co}, \text{Ni}$) Complexes with Strong Magnetic Exchange Giving Rise to Slow Magnetic Relaxation. *Chem. Sci.* **2020**, *11*, 8196–8203.
- (37) Huang, Z.; Grape, E. S.; Li, J.; Inge, A. K.; Zou, X. 3D Electron Diffraction as an Important Technique for Structure Elucidation of Metal–Organic Frameworks and Covalent Organic Frameworks. *Coord. Chem. Rev.* **2021**, *427*, 213583.

- (38) Trucano, P.; Chen, R. Structure of Graphite by Neutron Diffraction. *Nature* **1975**, *258*, 136–137.
- (39) Beamson, G.; Briggs, D. *High Resolution XPS of Organic Polymers: The Scienta ESCA 300 Database*; Wiley: New York, NY, 1992. Appendices 3.1 and 3.2.
- (40) Trotochaud, L.; Head, A. R.; Pletincx, S.; Karslıoğlu, O.; Yu, Y.; Waldner, A.; Kyhl, L.; Hauffman, T.; Terryn, H.; Eichhorn, B.; Bluhm, H. Water Adsorption and Dissociation on Polycrystalline Copper Oxides: Effects of Environmental Contamination and Experimental Protocol. *J. Phys. Chem. B* **2018**, *122*, 1000–1008.
- (41) Gu, S.; Du, J.; Huang, J.; Guo, Y.; Yang, L.; Xu, W.; Chen, W. Unsymmetrical NCN-Pincer Mononuclear and Dinuclear Nickel(II) Complexes of N-Heterocyclic Carbene (NHC): Synthesis, Structure and Catalysis for Suzuki–Miyaura Cross-Coupling. *Dalton Trans.* **2017**, *46*, 586–594.
- (42) Zhang, D.; Zhu, Y.; Liu, L.; Ying, X.; Hsiung, C.-E.; Sougrat, R.; Li, K.; Han, Y. Atomic-Resolution Transmission Electron Microscopy of Electron Beam-Sensitive Crystalline Materials. *Science* **2018**, *359*, 675–679.
- (43) Wang, L.; Ni, Y.; Hou, X.; Chen, L.; Li, F.; Chen, J. A Two-Dimensional Metal–Organic Polymer Enabled by Robust Nickel–Nitrogen and Hydrogen Bonds for Exceptional Sodium Ion Storage. *Angew. Chem., Int. Ed.* **2020**, *59*, 22126–22131.
- (44) Rietveld, H. M. A Profile Refinement Method for Nuclear and Magnetic Structures. *J. Appl. Crystallogr.* **1969**, *2*, 65–71.
- (45) Fratini, S.; Nikolka, M.; Salleo, A.; Schweicher, G.; Sirringhaus, H. Charge Transport in High-Mobility Conjugated Polymers and Molecular Semiconductors. *Nat. Mater.* **2020**, *19*, 491–502.
- (46) Anthony, J. E.; Brooks, J. S.; Eaton, D. L.; Parkin, S. R.; May, R. V. Functionalized Pentacene: Improved Electronic Properties from Control of Solid-State Order. *J. Am. Chem. Soc.* **2001**, *123*, 9482–9483.
- (47) Skorupskii, G.; Trump, B. A.; Kasel, T. W.; Brown, C. M.; Hendon, C. H.; Dincă, M. Efficient and Tunable One-Dimensional Charge Transport in Layered Lanthanide Metal–Organic Frameworks. *Nat. Chem.* **2020**, *12*, 131–136.
- (48) Schoedel, A.; Li, M.; Li, D.; O’Keeffe, M.; Yaghi, O. M. Structures of Metal–Organic Frameworks with Rod Secondary Building Units. *Chem. Rev.* **2016**, *116*, 12466–12535.
- (49) Wu, X.; Qiu, Y.; Chen, Z.; Guan, B.; Hao, X.; Rykov, A. I.; Sun, Y.; Liu, L.; Zou, Y.; Sun, J.; Xu, W.; Zhu, D. Paramagnetic Conducting Metal–Organic Frameworks with Three-Dimensional Structure. *Angew. Chem., Int. Ed.* **2020**, *59*, 20873–20878.
- (50) Chen, G.; Gee, L. B.; Xu, W.; Zhu, Y.; Lezama-pacheco, J. S.; Huang, Z.; Li, Z.; Babicz, J. T.; Choudhury, S.; Chang, T.-H.; Reed, E.; Solomon, E. I.; Bao, Z. Valence-Dependent Electrical Conductivity in a 3D Tetrahydroquinone-Based Metal–Organic Framework. *J. Am. Chem. Soc.* **2020**, *142*, 21243–21248.
- (51) Li, M.; Li, D.; O’Keeffe, M.; Yaghi, O. M. Topological Analysis of Metal–Organic Frameworks with Polytopic Linkers and/or Multiple Building Units and the Minimal Transitivity Principle. *Chem. Rev.* **2014**, *114*, 1343–1370.
- (52) Grosvenor, A. P.; Biesinger, M. C.; Smart, R. S. C.; McIntyre, N. S. New Interpretations of XPS Spectra of Nickel Metal and Oxides. *Surf. Sci.* **2006**, *600*, 1771–1779.
- (53) Stang, S.; Lebkücher, A.; Walter, P.; Kaifer, E.; Himmel, H. J. Redox-Active Guanidine Ligands with Pyridine and p-Benzoquinone Backbones. *Eur. J. Inorg. Chem.* **2012**, 4833–4845.
- (54) Masui, H.; Freda, A. L.; Zerner, M. C.; Lever, A. B. P. Binuclear 1,2,4,5-Tetraimino-3,6-Diketocyclohexane Bis[bis(bipyridine)-ruthenium(II)] Redox Series. *Inorg. Chem.* **2000**, *39*, 141–152.
- (55) Vlček, A., Jr. Metal and Ligand Oxidation States in Dioxolene Complexes: Meaning, Assignment and Control. *Comments Inorg. Chem.* **1994**, *16*, 207–228.
- (56) Bernard, M. C.; Goff, A. H. Raman Spectroscopy for the Study of Polyaniline. *Synth. Met.* **1997**, *85*, 1145–1146.
- (57) Siri, O.; Taquet, J.-p.; Collin, J.-P.; Rohmer, M.-M.; Bénard, M.; Braunstein, P. Tunable Charge Delocalization in Dinickel Quinonoid Complexes. *Chem. Eur. J.* **2005**, *11*, 7247–7253.
- (58) Taquet, J.-p.; Siri, O.; Braunstein, P.; Welter, R.; Pascal, B.; Cedex, F.-S.; Welter, R.; Pasteur, L.; Pascal, B.; Cedex, F.-S. Dinuclear Nickel and Palladium Complexes with Bridging Catalytic Oligomerization of Ethylene. *Inorg. Chem.* **2006**, *45*, 4668–4676.
- (59) Jeon, I.-R.; Park, J. G.; Xiao, D. J.; Harris, T. D. An Azophenine Radical-Bridged Fe₂ Single-Molecule Magnet with Record Magnetic Exchange Coupling. *J. Am. Chem. Soc.* **2013**, *135*, 16845–16848.
- (60) Amalric Popescu, D.; Herrmann, J.-M.; Ensuque, A.; Bozon-Verduraz, F. Nanosized Tin Dioxide: Spectroscopic (UV–VIS, NIR, EPR) and Electrical Conductivity Studies. *Phys. Chem. Chem. Phys.* **2001**, *3*, 2522–2530.
- (61) Ni-2D is not sufficiently stable to allow magnetometry measurements.
- (62) Herebian, D.; Wiegardt, K. E.; Neese, F. Analysis and Interpretation of Metal-Radical Coupling in a Series of Square Planar Nickel Complexes: Correlated Ab Initio and Density Functional Investigation of [Ni(L^{ISQ})₂] (L^{ISQ}: 3,5-Di-tert-butyl-o-diiminobenzo-semiquinonate(1-)). *J. Am. Chem. Soc.* **2003**, *125*, 10997–11005.
- (63) Chłopek, K.; Bothe, E.; Neese, F.; Weyhermüller, T.; Wiegardt, K. Molecular and Electronic Structures of Tetrahedral Complexes of Nickel and Cobalt Containing N,N'-Disubstituted, Bulky o-Diiminobenzo-semiquinonate (1-) π -Radical Ligands. *Inorg. Chem.* **2006**, *45*, 6298–6307.
- (64) Balch, A. L.; Holm, R. H. Complete Electron-Transfer Series of the [M-N₄] Type. *J. Am. Chem. Soc.* **1966**, *88*, S201–S209.
- (65) Bencini, A.; Carbonera, C.; Dei, A.; Vaz, M. G. F. Magnetic Exchange Interaction between Paramagnetic Transition Metal Ions and Radical Ligands. A 9,10-Dioxophenanthrenesemiquinonato Adduct of a Nickel(II)-Tetraazamacrocyclic Complex and DFT Description. *Dalton Trans.* **2003**, *9*, 1701–1706.
- (66) Skorupskii, G.; Dincă, M. Electrical Conductivity in a Porous, Cubic Rare-Earth Catecholate. *J. Am. Chem. Soc.* **2020**, *142*, 6920–6924.
- (67) Schwarze, M.; Gaul, C.; Scholz, R.; Bussolotti, F.; Hofacker, A.; Schellhammer, K. S.; Nell, B.; Naab, B. D.; Bao, Z.; Spoltore, D.; Vandewal, K.; Widmer, J.; Kera, S.; Ueno, N.; Ortmann, F.; Leo, K. Molecular Parameters Responsible for Thermally Activated Transport in Doped Organic Semiconductors. *Nat. Mater.* **2019**, *18*, 242–248.
- (68) Mott, N. F. Conduction in Glasses Containing Transition Metal Ions. *J. Non-Cryst. Solids* **1968**, *1*, 1–17.
- (69) Park, S. S.; Hontz, E. R.; Sun, L.; Hendon, C. H.; Walsh, A.; Van Voorhis, T.; Dincă, M. Cation-Dependent Intrinsic Electrical Conductivity in Isostructural Tetrathiafulvalene-Based Microporous Metal–Organic Frameworks. *J. Am. Chem. Soc.* **2015**, *137*, 1774–1777.
- (70) Xie, L. S.; Dincă, M. Novel Topology in Semiconducting Tetrathiafulvalene Lanthanide Metal–Organic Frameworks. *Isr. J. Chem.* **2018**, *58*, 1119–1122.
- (71) Ko, M.; Mendecki, L.; Eagleton, A. M.; Durbin, C. G.; Stolz, R. M.; Meng, Z.; Mirica, K. A. Employing Conductive Metal–Organic Frameworks for Voltammetric Detection of Neurochemicals. *J. Am. Chem. Soc.* **2020**, *142*, 11717–11733.